

# Deciphering the Dynamic Structure Evolution of Fe- and Ni-Codoped CoS<sub>2</sub> for Enhanced Water Oxidation

Wenfeng Peng, Amol Deshmukh, Ning Chen, Zhengxing Lv, Shijing Zhao, Jiong Li, Bingmin Yan, Xiang Gao, Lu Shang, Yutong Gong, Lailei Wu,\* Mingyang Chen,\* Tierui Zhang, and Huiyang Gou\*



Cite This: *ACS Catal.* 2022, 12, 3743–3751



Read Online

HPSTAR  
1572-2022

ACCESS |



Metrics & More



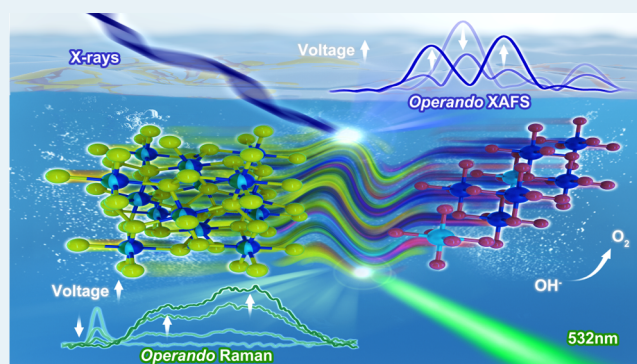
Article Recommendations



Supporting Information

**ABSTRACT:** Multimetal doping is a promising strategy to achieve high-performance electrocatalysts for the oxygen evolution reaction (OER) due to synergistic effects; however, understanding the dynamic structure evolution and clarifying the catalytic mechanism of each individual doping metal in multimetal-based electrocatalysts remain elusive. Here, we report the synthesis of homogeneous single-metal and bimetal doping sulfides with a pyrite structure for OER catalysts via a high-pressure and high-temperature (HPHT) technique; operando Raman and X-ray absorption spectroscopy (XAS) studies are performed to capture the dynamic evolution during the OER process. Our results find that an Fe- and Ni-codoped CoS<sub>2</sub> electrocatalyst exhibits significantly improved OER activity with an overpotential of 242 (295) mV at 10 (100) mA cm<sup>-2</sup> and robust stability over 500 h in an alkaline medium. Operando analysis reveals that Fe and Ni incorporations not only expedite the dynamic response of self-reconstructions of the Fe,Ni-CoS<sub>2</sub> surface but also accelerate the oxidation of Co and Fe into high-valence oxyhydroxides while suppressing nickel oxidation to form Ni(OH)<sub>2</sub> for optimized activity and robust stability. This finding provides a fundamental understanding of the composition design, dynamic reaction pathways, and controlling principle for highly active multimetal-based OER catalysts.

**KEYWORDS:** multimetal doping, high-pressure synthesis, operando characterization, dynamic structure evolutions, oxygen evolution reaction



## INTRODUCTION

Electrochemical water splitting to generate oxygen and hydrogen holds great potential for sustainable and clean energy conversion. However, the anodic half-reaction of the oxygen evolution reaction (OER) is a limiting process requiring a high electrochemical overpotential to overcome the kinetic barriers.<sup>1–3</sup> Therefore, the design and synthesis of highly active electrocatalysts to reduce the overpotential of OER are of fundamental importance for practical applications. Heteroatom doping engineering has been established as an alternative means for the realization of high-performance electrocatalysts.<sup>4–7</sup> Catalytically active 3d transition metals such as Fe, Co, and Ni are usually primary choices for heteroatom doping; extensive efforts to obtain advanced multimetal-based catalysts with diverse compositions and structures offer the fundamental understanding of their synthetic strategies and structure–composition–activity correlation.<sup>8–11</sup>

Pyrite-type transition metal sulfides have received growing attention as promising OER catalysts because of their earth abundance, controllable morphologies, and tunable electronic properties.<sup>12,13</sup> It is worth noting that heteroatom-doped

transition metal (Fe, Co, and Ni) sulfides, e.g., Ni-doped FeS<sub>2</sub>, Fe-doped NiS<sub>2</sub>, and V-doped NiS<sub>2</sub>, showed enhanced electronic conductivity and activity as compared to pristine sulfides.<sup>14–16</sup> From the crystallographic perspective, the highly symmetrical pyrite structure could provide sufficient heteroatom compatibility, allowing more heteroatoms to further improve the catalytic performance and identify the specific role of doping metals.<sup>17</sup> However, the lack of advanced synthesis and characterization techniques impedes the understanding of the interplay of doping metals with the host, the reconstruction process of metal doping, and the catalytic origin of pyrite-type sulfides. Here, we perform a high-pressure synthesis of single-metal and bimetal-doped CoS<sub>2</sub> as OER electrocatalysts.<sup>18</sup> Operando Raman and X-ray absorption spectroscopy (XAS) measurements were carried out to capture the dynamic surface

Received: January 19, 2022

Revised: February 22, 2022

Published: March 10, 2022



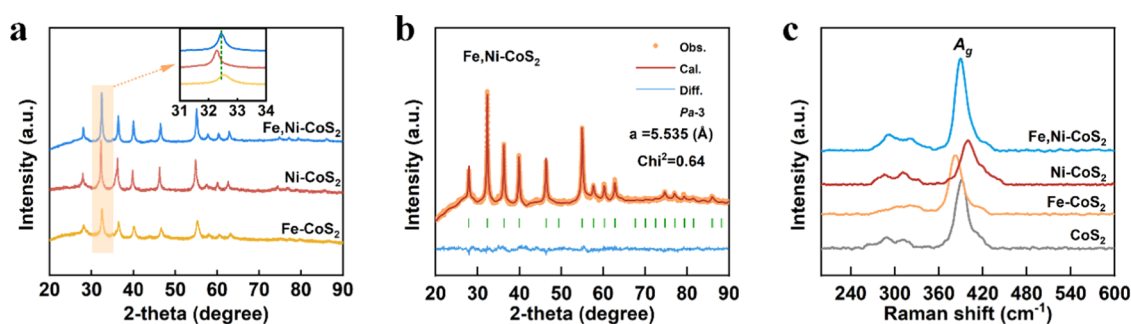


**Figure 1.** (a) Collected XRD patterns and the enlarged (200) diffraction planes of Fe,Ni-CoS<sub>2</sub>, Ni-CoS<sub>2</sub>, and Fe-CoS<sub>2</sub> with the pyrite structure. (b) Rietveld refinement of Fe,Ni-CoS<sub>2</sub>. (c) Collected micro-Raman spectra with a wavelength of 532 nm for Fe,Ni-CoS<sub>2</sub>, Ni-CoS<sub>2</sub>, Fe-CoS<sub>2</sub>, and CoS<sub>2</sub>.

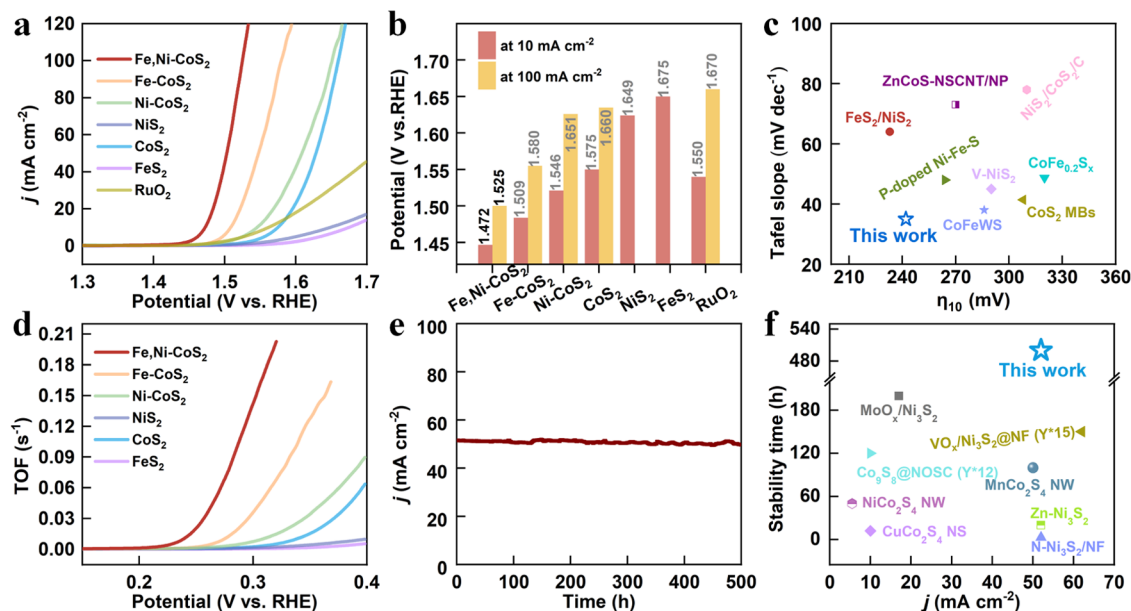


**Figure 2.** OER characterization of Fe,Ni-CoS<sub>2</sub>, Ni-CoS<sub>2</sub>, Fe-CoS<sub>2</sub>, CoS<sub>2</sub>, FeS<sub>2</sub>, NiS<sub>2</sub>, and RuO<sub>2</sub>. (a, b) LSV polarization curves and the corresponding OER potential (at 10 and 100 mA cm<sup>-2</sup>). (c) Overpotential ( $\eta_{10}$ ) and the Tafel slope of Fe,Ni-CoS<sub>2</sub> compared with those of the catalysts from the recent literature (Table S3). (d) TOFs of the as-prepared sulfide electrocatalysts. (e) Chronoamperometric curve of Fe,Ni-CoS<sub>2</sub> over 500 h in 1.0 M KOH at an overpotential of 285 mV and Fe,Ni-CoS<sub>2</sub> deposited on nickel foam without iR compensation. (f) Main stability parameters (time and current densities) of Fe,Ni-CoS<sub>2</sub> are compared with those of the recently reported earth-abundant sulfides electrocatalysts (Table S4).

reconstruction for highly active Fe- and Ni-codoped CoS<sub>2</sub>. The interactions between Fe or/and Ni and Co are revealed in details to establish an optimization principle for heteroatom substitution engineering.

## RESULTS AND DISCUSSION

Fe-doped CoS<sub>2</sub> (Co<sub>0.8</sub>Fe<sub>0.2</sub>S<sub>2</sub>, referred to as Fe-CoS<sub>2</sub>), Ni-doped CoS<sub>2</sub> (Co<sub>0.8</sub>Ni<sub>0.2</sub>S<sub>2</sub>, referred to as Ni-CoS<sub>2</sub>), Fe- and Ni-codoped CoS<sub>2</sub> (Co<sub>0.8</sub>Fe<sub>0.11</sub>Ni<sub>0.09</sub>S<sub>2</sub>, referred to as Fe,Ni-CoS<sub>2</sub>), and pristine CoS<sub>2</sub>, FeS<sub>2</sub>, and NiS<sub>2</sub> are synthesized under high-pressure high-temperature (HPHT) conditions (see the Experimental Section in the Supporting Information for details). The structures of the as-prepared samples were characterized using powder X-ray diffraction (XRD) shown in Figures 1a and S1. The obtained XRD patterns of Fe,Ni-CoS<sub>2</sub>, Fe-CoS<sub>2</sub>, and Ni-CoS<sub>2</sub> (Figure 1a) can be indexed into a pyrite-type structure (Space group: Pa3) without distinguishable impurity. The observed difference of the (200) plane of Fe,Ni-CoS<sub>2</sub>, Ni-CoS<sub>2</sub>, and Fe-CoS<sub>2</sub> is most likely due to the difference in intrinsic ionic radii of Fe, Co, and Ni, indicating

the successful doping of Fe or/and Ni into CoS<sub>2</sub> (inset of Figure 1a). The Rietveld refinements of XRD patterns for Fe,Ni-CoS<sub>2</sub> and CoS<sub>2</sub> are shown in Figures 1b and S2a. The obtained lattice parameter, 5.535 Å, for Fe,Ni-CoS<sub>2</sub> (Table S1) agrees well with the previous report (5.538 Å), close to that of CoS<sub>2</sub> (5.534 Å).<sup>19</sup> The confocal micro-Raman spectra of Fe,Ni-CoS<sub>2</sub>, Ni-CoS<sub>2</sub>, Fe-CoS<sub>2</sub>, and CoS<sub>2</sub> are shown in Figure 1c. The Raman modes of CoS<sub>2</sub>, E<sub>g</sub> (288 cm<sup>-1</sup>), T<sub>g</sub>(1) (312 cm<sup>-1</sup>), A<sub>g</sub> (390 cm<sup>-1</sup>), and T<sub>g</sub>(2) (414 cm<sup>-1</sup>), are observed (Figure S2b), consistent with previous results.<sup>20</sup> The spectrum of Fe,Ni-CoS<sub>2</sub> (Figure S2c) shows similar Raman vibrations as CoS<sub>2</sub> with a slight red shift, whereas the spectrum of Ni-CoS<sub>2</sub> (Fe-CoS<sub>2</sub>) exhibits a blue shift (red shift) relative to that of CoS<sub>2</sub> (Figure 1c). The distinctive A<sub>g</sub> peak suggests that the obtained Fe,Ni-CoS<sub>2</sub>, Ni-CoS<sub>2</sub>, and Fe-CoS<sub>2</sub> are homogeneous single-phase sulfides. Moreover, scanning electron microscopy (SEM, Figure S3) reveals common interacting nanoparticle features (ranging from tens to hundreds of nanometers). Energy-dispersive X-ray (EDX) analysis finds very uniform composition distributions and the stoichiometric ratio of CoS<sub>2</sub>, Ni-CoS<sub>2</sub>, Fe-CoS<sub>2</sub>, and Fe,Ni-CoS<sub>2</sub>, as shown in Figure S4 and

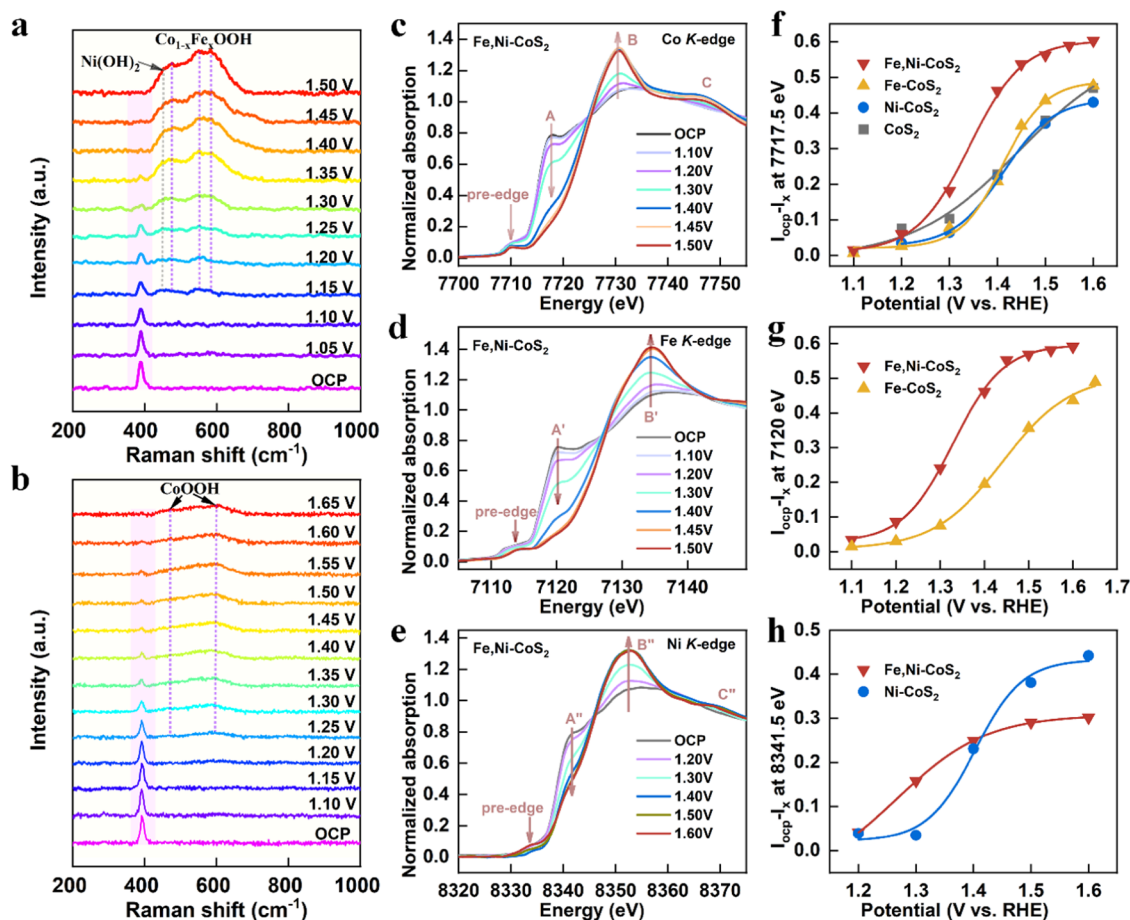


**Figure 3.** (a) Operando Raman spectra of Fe,Ni-CoS<sub>2</sub> (a) and CoS<sub>2</sub> (b) catalysts at various applied potentials (V vs RHE) in 1.0 M KOH. Operando Co (c), Fe (d), and Ni (e) K-edge X-ray absorption near edge structure (XANES) spectra of Fe,Ni-CoS<sub>2</sub> at varied potentials during the OER process. The evolution of the XANES ( $I_{\text{ocp}} - I_x$ ) at 7717.5 (f), 7120 (g), and 8341.5 (h) eV for Fe,Ni-CoS<sub>2</sub>, Fe-CoS<sub>2</sub>, Ni-CoS<sub>2</sub>, and CoS<sub>2</sub>. Solid lines represent the fittings by the Boltzmann equation.

**Table S2.** The high-resolution transmission electron microscopy (HRTEM) images (Figure S5) show a clear lattice fringe of 0.32 nm, corresponding to the (111) crystal plane of pyrite Fe,Ni-CoS<sub>2</sub>. In addition, the compositional mapping from TEM-EDX (Figure S5) also indicates the homogeneous distribution of the constituents (Fe, Co, Ni, and S).

The OER activity of the as-prepared catalysts supported on a glass carbon (GC) electrode (mass density is about 0.24 mg cm<sup>-2</sup>) was evaluated using a standard three-electrode system in an alkaline environment (1.0 M KOH). The *iR*-corrected OER polarization curves (Figure 2a) indicate that Fe,Ni-CoS<sub>2</sub>/GC exhibits a better catalytic performance with a very low overpotential of 242 (295) mV at 10 (100) mA cm<sup>-2</sup> ( $\eta_{10} = 242$  mV,  $\eta_{100} = 295$  mV, Figure 2b) than those of Fe-CoS<sub>2</sub>/GC ( $\eta_{10} = 279$  mV,  $\eta_{100} = 350$  mV), Ni-CoS<sub>2</sub>/GC ( $\eta_{10} = 316$  mV,  $\eta_{100} = 421$  mV), CoS<sub>2</sub>/GC ( $\eta_{10} = 345$  mV,  $\eta_{100} = 430$  mV), NiS<sub>2</sub>/GC ( $\eta_{10} = 419$  mV), FeS<sub>2</sub>/GC ( $\eta_{10} = 445$  mV), and RuO<sub>2</sub>/GC ( $\eta_{10} = 320$  mV,  $\eta_{100} = 440$  mV). LSV curves without *iR*-correction (Figure S6a) show similar OER performance trends. Furthermore, the catalytic kinetics of as-prepared catalysts were evaluated by the Tafel plots (Figure S6b), which reveals a smaller Tafel slope (35 mV dec<sup>-1</sup>) of Fe,Ni-CoS<sub>2</sub> than those of Fe-CoS<sub>2</sub> (39 mV dec<sup>-1</sup>), Ni-CoS<sub>2</sub> (66 mV dec<sup>-1</sup>), CoS<sub>2</sub> (61 mV dec<sup>-1</sup>), NiS<sub>2</sub> (115 mV dec<sup>-1</sup>), FeS<sub>2</sub> (102 mV dec<sup>-1</sup>), and RuO<sub>2</sub> (92 mV dec<sup>-1</sup>), indicating that Fe and Ni codoping can expedite OER kinetics

significantly. Judging from the overpotential ( $\eta_{10}$ ) and Tafel slopes, Fe,Ni-CoS<sub>2</sub> exhibits OER activity comparable to the state-of-the-art sulfide-based catalysts (Figure 2c and Table S3). Moreover, electrochemical impedance spectroscopy (EIS) was also performed to understand the reaction kinetics. As shown in Figure S7, Fe,Ni-CoS<sub>2</sub> has a smaller charge transfer resistance ( $R_{\text{ct}}$ , 6.87  $\Omega$ ) than those of other sulfides (Fe-CoS<sub>2</sub>: 39.3  $\Omega$ ; Ni-CoS<sub>2</sub>: 97.9  $\Omega$ ; CoS<sub>2</sub>: 323  $\Omega$ ; NiS<sub>2</sub>: 558  $\Omega$ ; FeS<sub>2</sub>: 1085  $\Omega$ ), suggesting the accelerated charge transfer by Fe and Ni codoping.<sup>21</sup> The electrochemical surface areas (ECSAs) were also evaluated by the electrochemical double-layer capacitance ( $C_{\text{dl}}$ ) because  $C_{\text{dl}}$  is linearly proportional to ECSA. The cyclic voltammetry current densities are collected at different scan rates in a non-faradic potential range (0.1–0.15 V), as shown in Figure S8a–d. The  $C_{\text{dl}}$  value of Fe,Ni-CoS<sub>2</sub> is 9.39 mF cm<sup>-2</sup> (Figure S8e), higher than those of Fe-CoS<sub>2</sub> (6.48 mF cm<sup>-2</sup>), Ni-CoS<sub>2</sub> (9.23 mF cm<sup>-2</sup>), and CoS<sub>2</sub> (8.07 mF cm<sup>-2</sup>), demonstrating that Fe and Ni codoping induces more active sites. The normalized activity of Fe,Ni-CoS<sub>2</sub> by ECSA is the highest among the studied catalysts (Figure S8f), indicating outstanding intrinsic OER activity. In addition, the mass activity (MA, Figure S9a) and turnover frequency (TOF, Figure 2d) of Fe,Ni-CoS<sub>2</sub> are also superior to those of Fe-CoS<sub>2</sub>, Ni-CoS<sub>2</sub>, CoS<sub>2</sub>, and NiS<sub>2</sub>, which further indicates its outstanding intrinsic OER activity. The faradic efficiency for Fe,Ni-CoS<sub>2</sub> is determined by the drainage

method (Figure S9b) and rotating ring-disk electrode (RRDE) measurement (Figure S9c, close to 100%), indicating high electron utilization efficiency. The electrocatalytic stability of Fe,Ni-CoS<sub>2</sub> deposited on nickel foam is evaluated by the continuous chronoamperometry test. The current–density remains robust stable (above 92%) after more than 500 h at an initial current–density of about 51.9 mA cm<sup>-2</sup> (the fixed overpotential of 285 mV), which exceeds most of the reported sulfide-based catalysts (Figure 2f and Table S4).

To probe the near-surface changes of catalysts, X-ray photoelectron spectroscopy (XPS) was carried out.<sup>22</sup> As compared with the original Fe,Ni-CoS<sub>2</sub>, the peak intensity of O 1s after OER is much greater (Figure S10), which suggests that more oxidized species were formed on the surface during the OER process. Furthermore, the surface reconstruction is also monitored by operando Raman measurements. When the electrodes (CoS<sub>2</sub>, Fe,Ni-CoS<sub>2</sub>) are immersed in the electrolyte (1.0 M KOH), there are no new peaks that show up [defined as open-circuit potential (OCP) in Figure 3a,b]. Characteristic Raman spectra of CoS<sub>2</sub> (Figure 3b) show no significant change until 1.2 V but a slight decrease of the A<sub>g</sub> peak intensity (the stretching of S<sub>2</sub><sup>2-</sup> dumbbells in CoS<sub>2</sub>).<sup>23</sup> With the increase in applied potential, the intensity of the A<sub>g</sub> peak reduced significantly, and two broad peaks belonging to CoOOH emerge from 1.25 V at about 480 and 600 cm<sup>-1</sup>.<sup>12</sup> The characteristic Raman peaks of CoOOH broaden and become stronger gradually as the potential increases, indicating a poor crystallinity or amorphous feature. Notably, the A<sub>g</sub> peak of Fe,Ni-CoS<sub>2</sub> (Figure 3a) disappears completely at 1.45 V, which is much lower than that of CoS<sub>2</sub> (1.65 V), indicating that Fe and Ni codoping facilitates the dynamic surface reconstruction. Simultaneously, Ni ions progressively evolve into β-Ni(OH)<sub>2</sub> with the characteristic Raman peak at 448 cm<sup>-1</sup>, as the applied potential increases.<sup>24</sup> Therefore, the observations prove that Fe and Ni codoping is more favorable for the generation of active species on the surface, which benefits OER catalytic activity.

Operando X-ray absorption spectroscopy (XAS) is performed to further track the dynamic structure evolutions in the electrocatalytic process. The schematic configuration of the electrochemical cell for the operando XAS setup is shown in Figure S11a,b. First, the stability of CoS<sub>2</sub> in an alkaline electrolyte (1.0 M KOH) is confirmed by the comparison of CoS<sub>2</sub>-OCP (immersion into the 1.0 M KOH electrolyte for 30 min) and pristine CoS<sub>2</sub> (Figure S11c). Then, multiple progressively proceeded XAS data are systematically collected throughout the in situ process. It is worth noting that Co, Fe, and Ni K-edge X-ray absorption near edge structure (XANES) spectra reveal a very similar evolution tendency as potentials vary throughout the OER process (Figure 3c–e), indicating a very close redox process. Figure 3c shows that the progressive increase in the intensity of the features of B and C is achieved at the expense of the intensity of the feature A, while what correspondingly revealed by the Fourier transform (FT) filtered  $\chi(k)$  is progressive inverting of the extended X-ray absorption fine structure (EXAFS) oscillation phases of c, d, and g, which are correlated to either the progressive peak position drifting and/or peak intensity changing for the extended EXAFS oscillation of a, b, e, f, h, i, and j (Figure S12a). Then, the starting and ending spectra of the in situ  $\chi(k)$  EXAFS are compared to standard spectra from Fe,Ni-CoS<sub>2</sub> and CoOOH models in XANES (Figure S12b) and EXAFS  $k^3\chi(k)$  (Figure S12c), respectively. Good agreement is found in the starting and ending status of data trends regarding A, B, and C

in XANES and a to j in EXAFS to those corresponding features possessed by Fe,Ni-CoS<sub>2</sub> and CoOOH, respectively, suggesting that the observed trends can be attributed to the progressive change in the partitioning ratio between end-member Co species of Fe,Ni-CoS<sub>2</sub> and CoOOH types throughout the in situ process. In addition, the experimental interpretation (the end member Co species of the in situ system possess Fe,Ni-CoS<sub>2</sub> and CoOOH types of the Co local structure) was further confirmed by the crystallography-guided XANES and EXAFS theoretical modeling using FDMNES and Feff7 codes for models of Fe, Ni-CoS<sub>2</sub>, and CoOOH (Figure S13).<sup>25,26</sup>

To address XANES data trends of A, B, and C (Figure 3c), XANES modeling is performed upon structure systems with Fe,Ni-CoS<sub>2</sub>-type and CoOOH-type structures. The radii of cluster compounds of two structure systems increase progressively from 3.0, 4.0, 5.0, 6.0, to 7.0 Å for the Fe,Ni-CoS<sub>2</sub>-type structure and from 3.0, 4.0, 5.0, to 6.0 Å for the CoOOH-type structure (Figure S14). The particle size effect on XAS modeling can be found in the Supporting Information. The Fe,Ni-CoS<sub>2</sub> structure based on XANES modeling ascribes the feature A to Co species of Fe,Ni-CoS<sub>2</sub> type (Figure S15a), consistent with the experimental observations and XANES modeling (Figure S13); the modeling further attributes the peak drifting of A to the progressive decreasing of the particle size of the Fe,Ni-CoS<sub>2</sub> type structure. In contrast, CoOOH structure-based XANES modeling further attributes features B and C to Co species with the CoOOH structure (Figure S15b), consistent with experiments. Furthermore, the modeling also reveals that the relative intensity of feature B is a fingerprint feature of extension of the CoOOH-type structure domain from two-dimensional (2D) to three-dimensional (3D), and the saturation in the intensity for C indicates the nanoscale of the CoOOH-type structure domain and beyond.

Based on the experimental observation and modeling (Figure S13), Fe,Ni-CoS<sub>2</sub> and CoOOH types of Co structures have been identified as end-member Co species in the sample with their partitioning weight changing progressively throughout the in situ process. Therefore, it is justifiable to select experimental data from Fe,Ni-CoS<sub>2</sub>-Co-OCP and CoOOH as standard spectra for linear combination fitting (LCF) analysis. Upon the detailed Discussion in the Supporting Information (named ‘possible error in LCF analysis’), namely XANES data from model compounds of Fe,Ni-CoS<sub>2</sub>-Co-OCP and CoOOH are justifiable as reliable standard spectra; the LCF analysis was performed for the in situ data system using the Athena code.<sup>27</sup> Fe,Ni-CoS<sub>2</sub>- and CoOOH-based LCF results in Table S5 and Figure S16 reveal that throughout the in situ system, the partitioning weight of the CoOOH-type structure is progressively increased at the expense of Fe,Ni-CoS<sub>2</sub>.

Furthermore, the comparison of K-edge XANES evolution for Co (Figures 3c and S17a–c), Fe (Figures 3d and S17d), and Ni (Figures 3e and S17e) in Fe,Ni-CoS<sub>2</sub>, Fe-CoS<sub>2</sub>, Ni-CoS<sub>2</sub>, and CoS<sub>2</sub> shows very different structure evolution rates as the applied potential changes. Therefore, we use the difference in the peak intensity ( $I_{\text{ocp}} - I_{\text{x}}$ ,  $I_{\text{ocp}}$  and  $I_{\text{x}}$  are the peak intensity at the same position (peak A: 7717.5 eV, peak A': 7120 eV, and peak A'': 8341.5 eV) of OCP and various potentials, respectively) to quantify the structure evolution of the redox process. The subtractive peak intensities of the peak A at 7717.5 eV for Fe,Ni-CoS<sub>2</sub>, Fe-CoS<sub>2</sub>, Ni-CoS<sub>2</sub>, and CoS<sub>2</sub> (Figure 3f) illustrate that Fe and Ni codoping can promote the surface Co ions into CoOOH more efficient than monoatomic doping, as evidenced by quite earliest transition, a faster

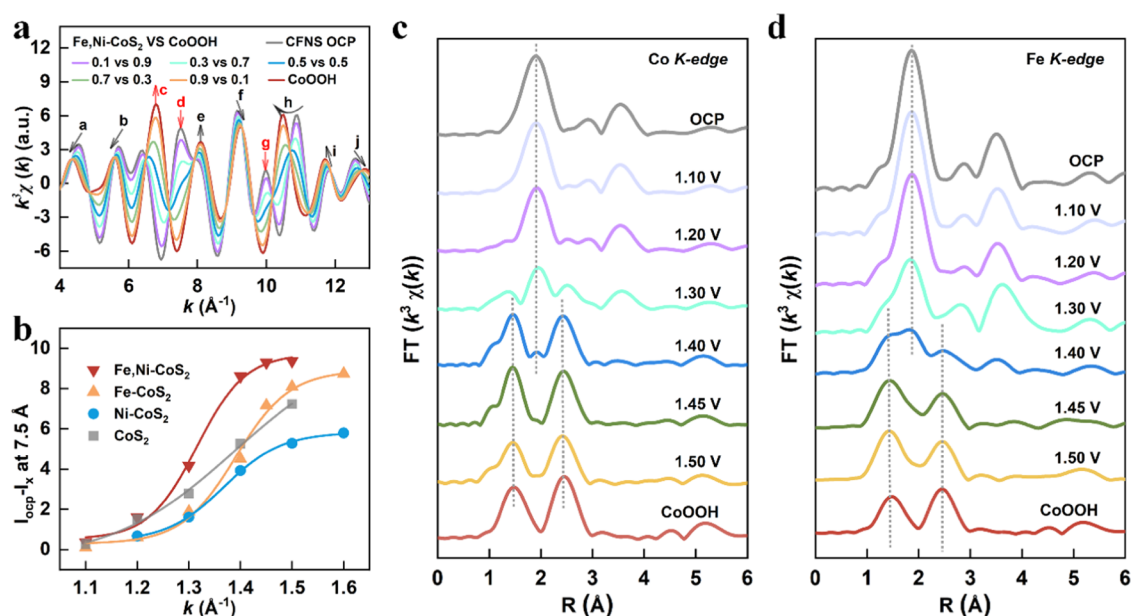


**Figure 4.** (a) Modeling performed with the partitioning ratio progressively changing between the BFT-filtered Fe,Ni-CoS<sub>2</sub>-OCP and CoOOH. (b) Evolution of the EXAFS  $k^3\chi(k)$  ( $I_{\text{ocp}} - I_x$ ) at fingerprint feature “d” for Fe,Ni-CoS<sub>2</sub>, Fe-CoS<sub>2</sub>, Ni-CoS<sub>2</sub>, and CoS<sub>2</sub>. Solid lines represent the fittings by the Boltzmann equation. (c) Co K-edge Fourier transformed  $k^3$ -weighted EXAFS of Fe,Ni-CoS<sub>2</sub> recorded at different potentials (FT range: 2.7–11.7 Å<sup>-1</sup>). (d) Fe K-edge Fourier transformed  $k^3$ -weighted EXAFS signals of Fe,Ni-CoS<sub>2</sub> recorded at different potentials (FT range: 2.9–11.3 Å<sup>-1</sup>).

transition rate, and greater transition accumulation. The comparison of the transition rate of Fe K-edge for Fe,Ni-CoS<sub>2</sub> and Fe-CoS<sub>2</sub> (Figure 3g) implies that the presence of Ni in Fe,Ni-CoS<sub>2</sub> facilitates the evolution of iron into higher than Fe<sup>3+</sup> (Figure S18). The difference of the transition rate of Ni K-edge in Fe,Ni-CoS<sub>2</sub> and Ni-CoS<sub>2</sub> (Figure 3h) supports the fact that the transition of Ni is decelerated by the evolution process of Fe, which may contribute to the excellent electrocatalytic stability.

EXAFS was further characterized by an in situ data system. The backward Fourier transform-filtered (BFT-filtered) EXAFS data from Fe,Ni-CoS<sub>2</sub> and CoOOH models are compared for their  $k^3\chi(k)$  (Figure S19), revealing corresponding EXAFS features of “a” to “j” possessed by the end-member spectra of the in situ data system. Guided by XANES analysis, the experimental  $k^3\chi(k)$  data system is modeled with the partitioning ratio progressively changing between Fe,Ni-CoS<sub>2</sub> and CoOOH (Figure 4a). The modeled  $k^3\chi(k)$  EXAFS data system successfully reproduced all experimental EXAFS features, including progressive data trends of “a”, “b”, “e”, “f”, “h”, “i”, and “j”, and oscillation phase progressive inverting trends of “c”, “d”, and “g”, related to the progressive transferring of the Co local structure from Fe,Ni-CoS<sub>2</sub> type to CoOOH type, supporting the XANES LCF analysis. Moreover, the subtractive characterization of peak intensities of trend “d” (at  $\sim 7.5$  Å<sup>-1</sup>) for Fe,Ni-CoS<sub>2</sub>, Fe-CoS<sub>2</sub>, Ni-CoS<sub>2</sub>, and CoS<sub>2</sub> (Figure 4b) shows almost the same evolution trend as observed by XANES (Figure 3f), which further confirms the progressively increased abundance of CoOOH in the in situ system. The Fourier transformed  $k^3$ -weighted operando EXAFS was carried out to further reveal the evolution of the local atomic environment. The EXAFS-FT results of Co K-edge for Fe,Ni-CoS<sub>2</sub> (Figure 4c) show that the Co–S (at about 1.90 Å) and Co–M peaks (M = Fe, Co, and Ni at about 3.53 Å) weaken as the potential increases; of particular interest, the avalanche effect occurs for the Co–S peak in Fe,Ni-CoS<sub>2</sub> when the potential is between 1.3 and 1.4 V. In this potential range,

two characteristic peaks of CoOOH (Co–O peak at about 1.45 Å and the Co–Co peak at about 2.42 Å) developed rapidly, indicating CoOOH increased rapidly at the expense of Fe,Ni-CoS<sub>2</sub>. Moreover, EXAFS curve fitting with modified Fe,Ni-CoS<sub>2</sub> and CoOOH structure models was performed to extract the coordination environment of absorbing Co, as shown in Figure S20 and Table S6. EXAFS fitting results (Table S6) of the Co K-edge data for Fe,Ni-CoS<sub>2</sub>-OCP confirm that the average S coordination number of the Co sites is approximately 6; however, the average coordination number of Co–S (Co–O) gradually decreases (increases) as the applied potential increases from 1.1 to 1.45 V. When the voltage increases from 1.45 to 1.5 V, the average O coordination number basically remains unchanged, which may indicate that the structural transformation of Fe,Ni-CoS<sub>2</sub> to CoOOH is basically completed within the detection depth; Also, the slight shortening of Co–O distances from 1.89 to 1.86 Å (1.45–1.50 V) indicates further increasing of the oxidation state of Co, consistent with Co K-edge XANES (Figure 3c,f). It is noted that the same trend of Fe K-edge EXAFS-FT for Fe,Ni-CoS<sub>2</sub> is also observed (Figure 4d); however, Fe sites are evolved into corresponding oxyhydroxide with two almost identical coordination peaks at about 1.45 and 2.42 Å, relative to the Co K-edge data for CoOOH, indicating the substitutional doped Fe in the CoOOH host with a higher-valence state due to the shorter Fe–O distances, consistent with Fe K-edge XANES (Figure S18).<sup>28</sup> On the basis of all of the abovementioned findings, we infer that Fe and Ni codoping can promote the Co/Fe ions into higher-valence state oxyhydroxides (Co<sub>1-x</sub>Fe<sub>x</sub>OOH) more efficiently than monatomic doping, which contributes to the enhanced OER catalytic activity. Simultaneously, the surface transition of Ni is decelerated by the evolution process of Fe, which may help for the excellent electrocatalytic stability.

To decipher the driving force of surface reconstruction, we evaluate the change in electronic states after Fe or/and Ni substitution using XAS (Figure S21); we can see that Co sites

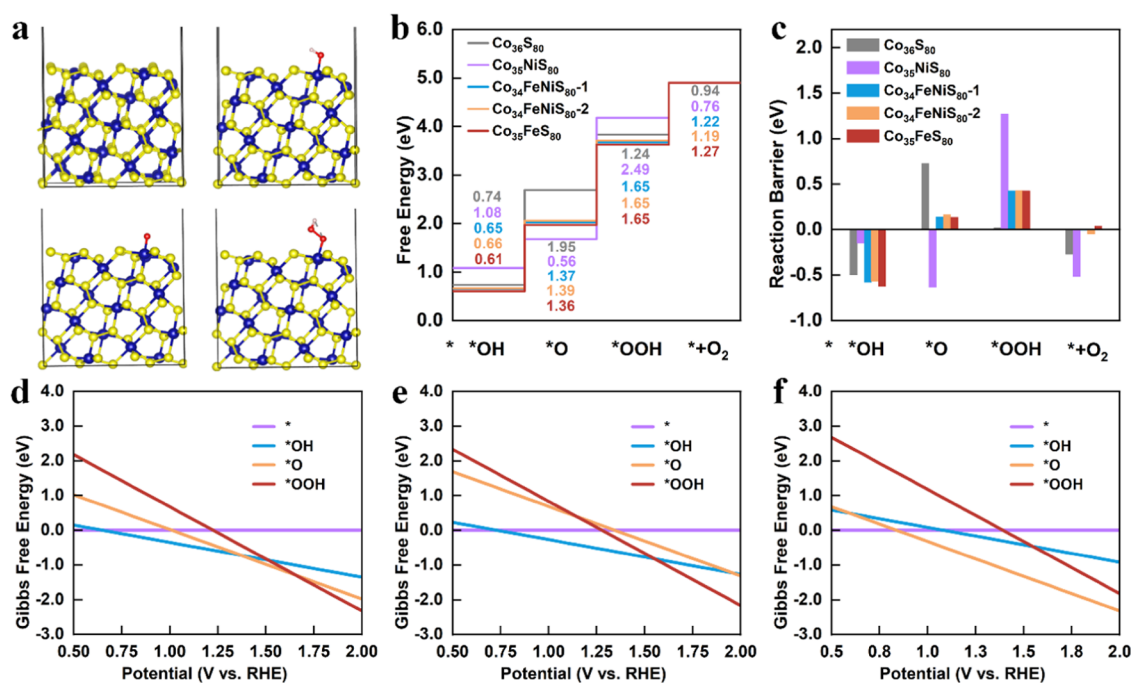


**Figure 5.** (a) \*, \*OH, \*O, and \*OOH OER intermediates at the Co site of the CoS<sub>2</sub> (102) surface. (b) Calculated OER profiles at the DFT level for the pure and doped CoS<sub>2</sub> (102) surfaces at an external bias of 0 V. The values next to the OER plots are energy barriers (reaction energies for elementary OER steps) at 0 V. The surface Co of CoS<sub>2</sub>, surface Fe of CoFeS<sub>2</sub>, surface Ni of CoNiS<sub>2</sub>, and surface Fe of two CoNiFeS<sub>2</sub> homotops (CoNiFeS<sub>2</sub>-1 and CoNiFeS<sub>2</sub>-2) are the considered catalytic sites. (c) Predicted reaction energies for elementary OER steps over the pure and doped CoS<sub>2</sub> (102) surfaces at an external bias of 1.23 V. The Gibbs free-energy evolution for \*, \*OH, \*O, and \*OOH as the function of the external bias vs RHE at (d) Fe of CoNiFeS<sub>2</sub>-1, (e) Co of CoS<sub>2</sub>, and (f) Ni of CoNiS<sub>2</sub>.

have an increasing valence state tendency: Ni-CoS<sub>2</sub> < CoS<sub>2</sub> < Fe-CoS<sub>2</sub> < Fe,Ni-CoS<sub>2</sub>, consistent with the XPS results (Figure S22); hence, we infer that metal ions with relatively more positive charge may lead to a facile structural transformation in sulfides.<sup>29</sup> Moreover, the changes in Fe and Ni valence states (Figure S21) also confirm our abovementioned hypothesis.

Density functional theory (DFT) calculations were also carried out to explain the different performances of pure and doped CoS<sub>2</sub> with Fe and Ni. OER energy profiles for catalytic sites on the (102) surface of pure and doped CoS<sub>2</sub> were predicted and are shown in Figure 5. The surface Co of CoS<sub>2</sub>, surface Fe of CoFeS<sub>2</sub>, surface Ni of CoNiS<sub>2</sub>, and surface Fe of two CoNiFeS<sub>2</sub> homotops are considered. The optimized geometries of the OER species (\*, \*OH, \*O, and \*OOH) for the pure and doped CoS<sub>2</sub> (102) slabs are shown in Figures S5a and S23. The OER energy profiles for the pure and doped CoS<sub>2</sub> under an external bias of 0 V are given in Figure 5b. The comparison of the OER elementary reaction barriers under an external bias of 1.23 V for the pure and doped CoS<sub>2</sub> (102) slabs is shown in Figure 5c. The OER reaction over the pure CoS<sub>2</sub> (102) slab (Co<sub>36</sub>S<sub>80</sub>) contributes to a theoretical overpotential  $\eta_{\text{DFT}}$  of 0.72 V, with \*OH → \*O being the rate-limiting step. For the Fe site of a Fe-doped CoS<sub>2</sub> (102) slab (Co<sub>35</sub>FeS<sub>80</sub>), the OER overpotential is improved to be 0.42 V (\*O → \*OOH), and \*OH → \*O is no longer the rate-limiting step with an energy barrier of 0.12 eV under a bias of 1.23 V. This indicates that the surface Fe dopant can serve as the high-activity site to enhance the OER performance. Conversely, for the Ni site of the Ni-doped CoS<sub>2</sub> (Co<sub>35</sub>NiS<sub>80</sub>), the overpotential is increased to 2.49 V with \*O → \*OOH being the rate-limiting step, due to too strong \*O adsorption and too weak \*OOH adsorption. The predicted catalytic activity of Fe and inactivity of Ni are consistent with

the experiment. A possible explanation for the significant differences in the OER activities of Fe and Ni is that Fe can readily reach oxidation states over +2, while Ni is innately frustrated at +3. In addition, codoping with Fe and Ni (Co<sub>34</sub>FeNiS<sub>80</sub>) leads to OER profiles similar to the Fe-doped CoS<sub>2</sub>, and the relative positions of the Fe and Ni dopants seem not to affect the OER performance (Figure 5c). This implies that in the slab model without defects, the adjacent Ni has negligible influence on the catalytic and electronic properties of Fe.

The OER activity of the Fe sites on the (011) and (111) surfaces of the Fe- and Ni-codoped CoS<sub>2</sub> was also predicted, as shown in Figures S24 and S25. The codoped CoS<sub>2</sub>(011) and Co<sub>30</sub>FeNiS<sub>60</sub>(111) exhibit theoretical overpotentials of 1.08 and 0.50 V, respectively. This implies that the population of the OER active sites might be quite high in Fe-CoS<sub>2</sub> and Fe,Ni-CoS<sub>2</sub>, contributed by different facets.

The predicted Gibbs free-energy evolution for the OER intermediates as the function of external bias vs RHE is given in Figure 5d–f for the typical surface Fe, Ni, and Co sites, respectively. The OER reaction is most efficient when the \*OH, \*O, and \*OOH intermediates are comparable in energy so that no overly stable intermediates are formed. Among Fe, Ni, and Co sites, only the energy evolution profile for the Fe site contains a narrow region (1.3–1.7 V vs RHE) that includes all of the intersections between the \*OH, \*O, and \*OOH profiles, suggesting the superior catalytic activity of the Fe site. Figure 5d–f also shows that the most thermally stable intermediate species changes subject to the applied bias. The dominant surface species at the Fe site is \*OH at a bias of 0.7–1.3 V, \*O at a bias of 1.3–1.6 V, and \*OOH at a bias of >1.6 V (Figure 5d). At the Co site, dominant surface species is predicted to be \*OH at a bias of 0.8–1.6 V and \*OOH at a

bias of  $>1.6$  V (Figure 5e). At Fe, the dominant  $^*OH$  at low voltage transitions into  $^*O$  when the external bias is increased to  $\sim 1.3$  V, and later transitions into  $^*OOH$ ; at Co,  $^*OH$  will be consumed at a higher bias ( $\sim 1.6$  V) due to the high thermal barrier toward  $^*O$ . The different thermodynamics for the OER intermediate surface species over the Fe and Co sites might account for the different surface oxidation rates of Fe-CoS<sub>2</sub> and Fe,Ni-CoS<sub>2</sub>, as revealed by the operando XAS. The Ni site is again found to be inactive, as the overly stable  $^*O$  will be formed on the surface to deactivate the OER process at a bias of  $>0.8$  V (Figure 5f), while the formation of  $^*O$  and  $^*OOH$  is not favorable. Although the abovementioned computational results are only for the (102) surface of the pure and doped CoS<sub>2</sub>, the revealed trends are in excellent agreement with the operando Raman and XAS results.

As found by the experiments, Fe,Ni-CoS<sub>2</sub> (Co<sub>0.8</sub>Fe<sub>0.11</sub>Ni<sub>0.09</sub>S<sub>2</sub>) exhibited the highest OER performance among the tested catalysts. The Ni dopant must play a role in enhancing the OER performance of Fe,Ni-CoS<sub>2</sub>, but the predicted OER profiles for the defectless Ni-CoS<sub>2</sub> slab suggest otherwise. To elucidate the synergetic effect of Ni, the structures and stabilities for the Co<sub>x</sub>Ni<sub>y</sub>Fe<sub>z</sub>S<sub>2</sub> compounds ( $x + y + z = 1$ ) are predicted using the first-principles calculations. The lattice deformation (%) for Co<sub>x</sub>Ni<sub>y</sub>Fe<sub>z</sub>S<sub>2</sub> as a function of  $x$ ,  $y$ , and  $z$  is plotted in a ternary contour diagram in Figure S26. The results show that increasing the Fe concentration reduces the lattice parameters of CoS<sub>2</sub>, whereas increasing the Ni concentration increases the lattice parameters. Hence, the single-metal doping of CoS<sub>2</sub> with Ni or Fe is likely to cause lattice mismatches between the doped and pure phases and lower the stability. Interestingly, when the Ni and Fe concentrations are approximately equal, Co<sub>x</sub>Ni<sub>y</sub>Fe<sub>z</sub>S<sub>2</sub> exhibits lattice parameters approximately equal to the lattice parameters of CoS<sub>2</sub>. The excellent electronic properties and OER performance of Fe,Ni-CoS<sub>2</sub> could be due to its uniform lattice to avoid the defective material structure such as stacking fault and dislocation.

Since the codoping of Fe and Ni is conducive for OER performance and a high codoping concentration does not cause the deformation of CoS<sub>2</sub>, is it possible to obtain a 1:1 Fe- and Ni-codoped CoS<sub>2</sub> with a high Fe (active site) concentration? To answer this question, the formation energy  $E_{\text{form}}$  as a function of  $x$ ,  $y$ , and  $z$  for Co<sub>x</sub>Ni<sub>y</sub>Fe<sub>z</sub>S<sub>2</sub> is evaluated and plotted in a ternary contour diagram in Figure S26. The results show that the stability of Co<sub>x</sub>Ni<sub>y</sub>Fe<sub>z</sub>S<sub>2</sub> decreases rapidly as the Co concentration is lowered, especially when the Ni and Fe concentrations are approximately equal. This implies that further improvement of Fe,Ni-CoS<sub>2</sub> by increasing the doping concentration could be thermodynamically challenging, which might be only achievable with nonregular synthesis such as HPHT.

## CONCLUSIONS

In summary, we have successfully synthesized a series of Fe- and/or Ni-doped CoS<sub>2</sub> as OER catalysts via an HPHT technique and systematically studied the effect of metal doping on their surface reconstruction and catalytic activity. Interestingly, Fe- and Ni-codoped CoS<sub>2</sub> exhibits the most remarkable OER performance and stability. Operando Raman and XAS studies demonstrated Fe and Ni codoping substantially promotes the surface Co and Fe transformation into higher-valence oxyhydroxides (Co<sub>1-x</sub>Fe<sub>x</sub>OOH) as highly active species, which contributes to the outstanding OER

activity. Meanwhile, the oxidation of Ni ions was suppressed to maintain excellent stability. This work offers a significant advancement in understanding the in situ evolution of active species and designing highly active multimetal-based OER catalysts.

## ASSOCIATED CONTENT

### Supporting Information

The Supporting Information is available free of charge at <https://pubs.acs.org/doi/10.1021/acscatal.2c00328>.

Experimental procedures (synthesis, characterization, and electrochemical measurement) and computational details (P2–10) and additional results of XRD, Raman, SEM, TEM, Tafel slopes, EIS, ECSA, MA, XPS, XAS, and computational details (Figures S1–S26) and (Table S1–S6) (PDF)

## AUTHOR INFORMATION

### Corresponding Authors

Lailei Wu – Yanshan University, Qinhuangdao 066004, China; Email: [wll@ysu.edu.cn](mailto:wll@ysu.edu.cn)

Mingyang Chen – Computational Science Research Center, Beijing 100193, China; Center for Green Innovation, School of Materials Science and Engineering, University of Science and Technology Beijing, Beijing 100083, China; Shunde Graduate School of University of Science and Technology Beijing, Foshan 528000, China; [orcid.org/0000-0002-9866-8695](https://orcid.org/0000-0002-9866-8695); Email: [mychen@ustb.edu.cn](mailto:mychen@ustb.edu.cn)

Huiyang Gou – Center for High Pressure Science and Technology Advanced Research, Beijing 100094, China; [orcid.org/0000-0002-2612-4314](https://orcid.org/0000-0002-2612-4314); Email: [huiyang.gou@hpstar.ac.cn](mailto:huiyang.gou@hpstar.ac.cn)

### Authors

Wenfeng Peng – Center for High Pressure Science and Technology Advanced Research, Beijing 100094, China

Amol Deshmukh – Computational Science Research Center, Beijing 100193, China; [orcid.org/0000-0003-0435-2196](https://orcid.org/0000-0003-0435-2196)

Ning Chen – Canadian Light Source, Saskatoon, Saskatchewan S7N2V3, Canada; [orcid.org/0000-0002-1269-6119](https://orcid.org/0000-0002-1269-6119)

Zhengxing Lv – Shanghai Synchrotron Radiation Facility, Shanghai 201210, China

Shijing Zhao – Center for High Pressure Science and Technology Advanced Research, Beijing 100094, China

Jiong Li – Shanghai Synchrotron Radiation Facility, Shanghai 201210, China; [orcid.org/0000-0001-6826-9987](https://orcid.org/0000-0001-6826-9987)

Bingmin Yan – Center for High Pressure Science and Technology Advanced Research, Beijing 100094, China

Xiang Gao – Center for High Pressure Science and Technology Advanced Research, Beijing 100094, China; [orcid.org/0000-0002-7496-158X](https://orcid.org/0000-0002-7496-158X)

Lu Shang – Key Laboratory of Photochemical Conversion and Optoelectronic Materials, Technical Institute of Physics and Chemistry, Chinese Academy of Sciences, Beijing 100190, China

Yutong Gong – State Key Laboratory of Solidification Processing, Northwestern Polytechnical University, Xi'an 710072 Shaanxi, China; [orcid.org/0000-0003-4676-9547](https://orcid.org/0000-0003-4676-9547)

Tierui Zhang – Key Laboratory of Photochemical Conversion and Optoelectronic Materials, Technical Institute of Physics

and Chemistry, Chinese Academy of Sciences, Beijing 100190, China; [orcid.org/0000-0002-7948-9413](https://orcid.org/0000-0002-7948-9413)

Complete contact information is available at:  
<https://pubs.acs.org/10.1021/acscatal.2c00328>

### Author Contributions

W.P. and A.D. contributed equally to this work.

### Funding

The National Natural Science Foundation of China (U1930401) and the Scientific and Technological Innovation Foundation of Shunde Graduate School, USTB (BK19BE024).

### Notes

The authors declare no competing financial interest.

## ACKNOWLEDGMENTS

The authors acknowledge the financial support from the National Natural Science Foundation of China (U1930401) and the Scientific and Technological Innovation Foundation of Shunde Graduate School, USTB (BK19BE024). The computational work was supported by the Tianhe2-JK computing time award at the Beijing Computational Science Research Center (CSRC). The authors thank beamline BL11B of the Shanghai Synchrotron Radiation Facility and Hard X-ray MicroAnalysis (HXMA) beamline Light Source (CLS) in Canada for providing the beamtime.

## REFERENCES

- (1) Seh, Z. W.; Kibsgaard, J.; Dickens, C. F.; Chorkendorff, I. B.; Nørskov, J. K.; Jaramillo, T. F. Combining theory and experiment in electrocatalysis: Insights into materials design. *Science* **2017**, *355*, No. eaad4998.
- (2) Feng, C.; Faheem, M. B.; Fu, J.; Xiao, Y.; Li, C.; Li, Y. Fe-based electrocatalysts for oxygen evolution reaction: progress and perspectives. *ACS Catal.* **2020**, *10*, 4019–4047.
- (3) Liang, C.; Zou, P.; Nairan, A.; Zhang, Y.; Liu, J.; Liu, K.; Yang, C.; et al. Exceptional performance of hierarchical Ni-Fe oxyhydroxide@NiFe alloy nanowire array electrocatalysts for large current density water splitting. *Energy Environ. Sci.* **2020**, *13*, 86–95.
- (4) Song, B.; Li, K.; Yin, Y.; Wu, T.; Dang, L.; Cabán-Acevedo, M.; Han, J.; Gao, T.; Wang, X.; Zhang, Z.; Schmidt, J. R.; Xu, P.; Jin, S. Tuning mixed nickel iron phosphosulfide nanosheet electrocatalysts for enhanced hydrogen and oxygen evolution. *ACS Catal.* **2017**, *7*, 8549–8557.
- (5) Burke, M. S.; Kast, M. G.; Trotochaud, L.; Smith, A. M.; Boettcher, S. W. Cobalt-iron (oxy) hydroxide oxygen evolution electrocatalysts: the role of structure and composition on activity, stability, and mechanism. *J. Am. Chem. Soc.* **2015**, *137*, 3638–3648.
- (6) Zhuo, J.; Cabán-Acevedo, M.; Liang, H.; Samad, L.; Ding, Q.; Fu, Y.; Li, M.; Jin, S. High-performance electrocatalysis for hydrogen evolution reaction using Se-doped pyrite-phase nickel diphosphide nanostructures. *ACS Catal.* **2015**, *5*, 6355–6361.
- (7) Li, M.; Gu, Y.; Chang, Y.; Gu, X.; Tian, J.; Wu, X.; Feng, L. Iron doped cobalt fluoride derived from CoFe layered double hydroxide for efficient oxygen evolution reaction. *Chem. Eng. J.* **2021**, *425*, No. 130686.
- (8) Zhang, X.; Zhang, X.; Xu, H.; Wu, Z.; Wang, H.; Liang, Y. Iron-doped cobalt monophosphide nanosheet/carbon nanotube hybrids as active and stable electrocatalysts for water splitting. *Adv. Funct. Mater.* **2017**, *27*, No. 1606635.
- (9) Xu, X.; Su, C.; Zhou, W.; Zhu, Y.; Chen, Y.; Shao, Z. Co-doping Strategy for Developing Perovskite Oxides as Highly Efficient Electrocatalysts for Oxygen Evolution Reaction. *Adv. Sci.* **2016**, *3*, No. 1500187.
- (10) Lee, S.; Bai, L.; Hu, X. Deciphering iron-dependent activity in oxygen evolution catalyzed by nickel-iron layered double hydroxide. *Angew. Chem., Int. Ed.* **2020**, *59*, 8072–8077.
- (11) He, R.; Li, M.; Qiao, W.; Feng, L. Fe doped Mo/Te nanorods with improved stability for oxygen evolution reaction. *Chem. Eng. J.* **2021**, *423*, No. 130168.
- (12) Han, X.; Wu, X.; Deng, Y.; Liu, J.; Lu, J.; Zhong, C.; Hu, W. Electrocatalysis: Ultrafine Pt Nanoparticle-Decorated Pyrite-Type CoS<sub>2</sub> Nanosheet Arrays Coated on Carbon Cloth as a Bifunctional Electrode for Overall Water Splitting. *Adv. Energy Mater.* **2018**, *8*, No. 1870110.
- (13) Hao, J.; Luo, W.; Yang, W.; Li, L.; Shi, W. Origin of the enhanced oxygen evolution reaction activity and stability of a nitrogen and cerium co-doped CoS<sub>2</sub> electrocatalyst. *J. Mater. Chem. A* **2020**, *8*, 22694–22702.
- (14) Dai, W.; Pan, Y.; Ren, K.; Zhu, Y. A.; Lu, T. Heteroatom Ni alloyed pyrite-phase FeS<sub>2</sub> as a pre-catalyst for enhanced oxygen evolution reaction. *Electrochim. Acta* **2020**, *355*, No. 136821.
- (15) Ding, X.; Li, W.; Kuang, H.; Qu, M.; Cui, M.; Zhao, C.; Qi, D. C.; Oropeza, F. E.; Zhang, K. H. An Fe stabilized metallic phase of NiS<sub>2</sub> for the highly efficient oxygen evolution reaction. *Nanoscale* **2019**, *11*, 23217–23225.
- (16) Liu, H.; He, Q.; Jiang, H.; Lin, Y.; Zhang, Y.; Habib, M.; Chen, S.; Song, L. Electronic structure reconfiguration toward pyrite NiS<sub>2</sub> via engineered heteroatom defect boosting overall water splitting. *ACS Nano* **2017**, *11*, 11574–11583.
- (17) Peng, W.; Li, J.; Shen, K.; Zheng, L.; Tang, H.; Gong, Y.; Zhou, J.; Chen, N.; Zhao, S.; Chen, M.; Gao, F.; Gou, H. Iron-regulated NiPS for enhanced oxygen evolution efficiency. *J. Mater. Chem. A* **2020**, *8*, 23580–23589.
- (18) Qin, G.; Wu, L.; Gou, H. Diamane: design, synthesis, properties, and challenges. *Funct. Diamond* **2021**, *1*, 83–92.
- (19) Pratt, J. L.; Bayliss, P. Crystal-structure refinement of cattierite. *Z. Kristallogr.* **1979**, *150*, 163–168.
- (20) Zhu, L.; Susac, D.; Teo, M.; Wong, K. C.; Wong, P. C.; Parsons, R. R.; Campbell, S. A.; et al. Investigation of CoS<sub>2</sub>-based thin films as model catalysts for the oxygen reduction reaction. *J. Catal.* **2008**, *258*, 235–242.
- (21) Wang, M.; Dong, C. L.; Huang, Y. C.; Shen, S. Operando spectral and electrochemical investigation into the heterophase stimulated active species transformation in transition-metal sulfides for efficient electrocatalytic oxygen evolution. *ACS Catal.* **2020**, *10*, 1855–1864.
- (22) Shao, G.; Peng, W.; Ma, C.; Zhao, W.; Guo, J.; Feng, Y.; Wang, H.; Zhang, R.; An, L. Enhanced electric conductivity of polymer-derived SiCN ceramics by microwave post-treatment. *J. Am. Ceram. Soc.* **2017**, *100*, 842–847.
- (23) Cabán-Acevedo, M.; Stone, M. L.; Schmidt, J. R.; Thomas, J. G.; Ding, Q.; Chang, H. C.; Tsai, M.; He, J.; Jin, S. Efficient hydrogen evolution catalysis using ternary pyrite-type cobalt phosphosulfide. *Nat. Mater.* **2015**, *14*, 1245–1251.
- (24) Klaus, S.; Cai, Y.; Louie, M. W.; Trotochaud, L.; Bell, A. T. Effects of Fe electrolyte impurities on Ni(OH)<sub>2</sub>/NiOOH structure and oxygen evolution activity. *J. Phys. Chem. C* **2015**, *119*, 7243–7254.
- (25) Joly, Y. X-ray absorption near-edge structure calculations beyond the muffin-tin approximation. *Phys. Rev. B* **2001**, *63*, No. 125120.
- (26) Ravel, B.; Newville, M. ATHENA, ARTEMIS, HEPHAESTUS: data analysis for X-ray absorption spectroscopy using IFEFFIT. *J. Synchrotron Radiat.* **2005**, *12*, 537–541.
- (27) Rehr, J. J.; Albers, R. C. Theoretical approaches to x-ray absorption fine structure. *Rev. Mod. Phys.* **2000**, *72*, 621.
- (28) Jiang, J.; Sun, F.; Zhou, S.; Hu, W.; Zhang, H.; Dong, J.; Jiang, Z.; Zhao, J.; Li, J.; Yan, W.; Wang, M. Atomic-level insight into super-efficient electrocatalytic oxygen evolution on iron and vanadium co-doped nickel (oxy) hydroxide. *Nat. Commun.* **2018**, *9*, No. 2885.
- (29) Yoon, T.; Kim, K. S. One-Step Synthesis of CoS-Doped β-Co(OH)<sub>2</sub>@Amorphous MoS<sub>2+x</sub> Hybrid Catalyst Growth on Nickel

Foam for High-Performance Electrochemical Overall Water Splitting.  
*Adv. Funct. Mater.* **2016**, *26*, 7386–7393.

## Recommended by ACS

---

### High-Entropy Alloy with Mo-Coordination as Efficient Electrocatalyst for Oxygen Evolution Reaction

Yunjie Mei, Jue Hu, *et al.*

AUGUST 19, 2022  
ACS CATALYSIS

READ 

---

### Co-Fe-P Nanosheet Arrays as a Highly Synergistic and Efficient Electrocatalyst for Oxygen Evolution Reaction

Yanyu Xie, Cheng-Yong Su, *et al.*

MAY 18, 2022  
INORGANIC CHEMISTRY

READ 

---

### Earth-Abundant Fe and Ni Dually Doped Co<sub>2</sub>P for Superior Oxygen Evolution Reactivity and as a Bifunctional Electrocatalyst toward Renewable Energy-Powered Overa...

Jiangtian Li, Rongzhong Jiang, *et al.*

SEPTEMBER 13, 2021  
ACS APPLIED ENERGY MATERIALS

READ 

---

### Nickel Iron Phosphide/Phosphate as an Oxygen Bifunctional Electrocatalyst for High-Power-Density Rechargeable Zn-Air Batteries

Neha Thakur, Tharamani C. Nagaiah, *et al.*

OCTOBER 28, 2021  
ACS APPLIED MATERIALS & INTERFACES

READ 

---

Get More Suggestions >

---